ELSEVIER

Journal of Fluids and Structures 24 (2008) 605–627

JOURNAL OF FLUIDS AND STRUCTURES

www.elsevier.com/locate/jfs

Near-wake flow characteristics of a circular cylinder close to a wall

X.K. Wang*, S.K. Tan

Maritime Research Centre, Nanyang Technological University, Singapore 639798, Singapore

Received 24 January 2007; accepted 7 November 2007
Available online 21 December 2007

Abstract

Flow characteristics in the near wake of a circular cylinder located close to a fully developed turbulent boundary layer are investigated experimentally using particle image velocimetry (PIV). The Reynolds number based on the cylinder diameter (D) is 1.2×10^4 and the incident boundary layer thickness (δ) is $0.4D$. Detailed velocity and vorticity fields in the wake region ($0 < x/D < 6$) are given for various gap heights (S) between the cylinder and the wall, with S/D ranging from 0.1 to 1.0. Both the ensemble-averaged (including the mean velocity vectors and Reynolds stress) and the instantaneous flow fields are strongly dependent on S/D. Results reveal that for $S/D \geqslant 0.3$, the flow is characterized by the periodic, Kármán-like vortex shedding from the upper and lower sides of the cylinder. The shed vortices and their evolution are revealed by analyzing the instantaneous flow fields using various vortex identification methods, including Galilean decomposition of velocity vectors, calculation of vorticity and swirling strength. For small and intermediate gap ratios ($S/D \leqslant 0.6$), the wake flow develops a distinct asymmetry about the cylinder centreline; however, some flow quantities, such as the Strouhal number and the convection velocity of the shed vortex, keep roughly constant and virtually independent of S/D.

Keywords: Vortex shedding; Cylinder; Boundary layer; Particle image velocimetry (PIV)

1. Introduction

There are many practical examples where cylindrical structures close to a solid wall are subjected to a cross-flow, for example pipelines on a seabed (Price et al., 2002). When a cylinder is placed near a wall, the near-wake flow characteristics, most notably the vortex shedding, will depend on the Reynolds number (Re), the gap height (S), and the characteristics of the incident boundary layer, etc.

Due to the engineering relevance of this flow, there are a large number of studies (mostly experimental measurements as listed in Table 1) in the literature. It is noted that most of the studies have been carried out at Reynolds numbers in the sub-critical regime $\mathrm{Re} = \mathcal{O}(10^4)$, in which the vortex shedding is relatively insensitive to Re. Flow visualization is the most straightforward method for observing the vortex shedding, and presents the physical process in detail [e.g. Grass et al., 1984]. However, the visualization experiments can, at best, provide qualitative estimates due to the dye diffusion.

*Corresponding author. Tel.: +65 6790 4874; fax: +65 6790 6620.
E-mail address: cxkwang@ntu.edu.sg (X.K. Wang).

0889-9746/$ - see front matter © 2007 Elsevier Ltd. All rights reserved.
doi:10.1016/j.jfluidstructs.2007.11.001

Table 1
Summary of previous experimental studies on a circular cylinder close to a wall

Author	Measurement technique	Re	δ/D	$(S/D)_{crit}$
Bearman and Zdravkovich (1978)	Pressure, hot-wire	$2.5-4.5\times10^4$	0.8	0.3
Grass et al. (1984)	Visualization, hot-film	1785, 3570	0.28, 2.6, 6	0.3 for $\delta/D<2.5$; 0.5 for $\delta/D\geqslant3.5$
Taniguchi and Miyakoshi (1990)	Load cell, pressure, hot-wire	9.4×10^4	0.34–1.05	0.3–0.9
Buresti and Lanciotti (1992)	Load cell	$0.88-2.77\times10^5$	0.1–1.1	0.4
Lei et al. (1999)	Pressure	$1.3-1.45\times10^4$	0.14–2.89	0.4–0.2
Choi and Lee (2000)	Visualization, pressure, hot-wire	1.4×10^4	0.35	0.3
Price et al. (2002)	Visualization, hot-film, PIV	1200–4960	0.36	0.5
Present	PIV	1.2×10^4	0.4	0.3

Therefore, the vortex shedding is often monitored with indirect methods in practice, such as hot-wire measurement [e.g. Bearman and Zdravkovich, 1978]. By analysing the spectra of hot-wire signals taken in the near wake of the cylinder, the strength and frequency of the vortex shedding can be determined. In some studies, the vortex shedding is also measured by strain gauge which gives the fluctuating lift [e.g. Buresti and Lanciotti, 1992]. Lei et al. (1999) observed three different flow regimes by examining the root-mean-square (rms) value of the lift coefficient: (i) a far wall regime where the flow and shedding characteristics are similar to the classical (no-wall) case; (ii) a wall regime for which the strength of vortex shedding and force fluctuations decrease as S is reduced to the critical gap height; and (iii) a suppressed regime where periodic fluctuations are no longer observed.

It is also shown that the critical gap height is dependent on the incident boundary layer thickness (δ). Bearman and Zdravkovich (1978) investigated the influence of S on the vortex shedding and spectral behaviour of the wake with a boundary layer thickness $\delta/D=0.8$. It was shown that when the gap-to-diameter ratio (i.e. S/D, abbreviated hereafter as gap ratio) is larger than 0.3, vortex shedding occurs; and shedding is suppressed when $S/D<0.3$. According to Grass et al. (1984), the critical gap ratio, $(S/D)_{crit}$, is about 0.3 as long as $\delta/D<2.5$, whereas it increases to about 0.5 for $\delta/D\geqslant3.5$. Taniguchi and Miyakoshi (1990) showed that $(S/D)_{crit}$ gradually increases with the increase of δ, that is, from $(S/D)_{crit}=0.3$ for $\delta/D\approx0.4$ to $(S/D)_{crit}=0.9$ for $\delta/D\approx1$. In contrast, Lei et al. (1999) showed that $(S/D)_{crit}$ decreases from 0.4 to 0.2, as δ/D increases from 0.14 to 2.89. Price et al. (2002) showed that the onset of vortex shedding can only be observed for $S/D\geqslant0.5$, while it is completely suppressed when $S/D\leqslant0.125$. In the intermediate region, $0.125<S/D<0.5$, the flow is similar to that for $S/D\leqslant0.125$, but there is a pronounced pairing between the lower shear layer shed from the bottom side of the cylinder and the wall boundary layer. A summary of some previous experimental studies on this flow configuration is given in Table 1.

The effect of the wall proximity on the vortex shedding frequency (f) is another well-studied research topic in the literature, where f was generally determined as the predominant peak in the power spectrum of lift (or drag), or that of velocity. Most studies, including those by Bearman and Zdravkovich (1978), Angrilli et al. (1982), Taniguchi and Miyakoshi (1990), Buresti and Lanciotti (1992), Lei et al. (1999) and Choi and Lee (2000), showed that f is insensitive to S/D, once vortex shedding takes place. The Strouhal number, $St=fD/U$, remains constant at about 0.2 and is identical with that in a uniform (no-wall) flow. On the other hand, several studies reported a tendency that the Strouhal number increases with decreasing S/D when the gap heights are small. Grass at al. (1984) reported that f tends to slightly increase as S/D decreases, and the maximum increase is about 10% for $S/D=0.5$. Price et al. (2002) found that when $S/D\leqslant0.25$, St can be as high as 0.4.

The above review indicates that there still remain some uncertainties regarding this flow configuration. Therefore, there exists a need for a robust experimental database on the wake flow structure to enhance physical understanding, as well as to facilitate code validation on the subject. It is noted that most of the previous experimental studies rely on flow visualization or point measurements (hot-wire or hot-film). In comparison, the present study employed particle image velocimetry (PIV) as the measurement technique, which allows for capturing the whole-field quantitative features. For instance, Dipankar and Sengupta (2005) conducted a computational study on this flow configuration using the concept of "instantaneous" vortex-induced stability to solve the Navier–Stokes equations. Two gap ratios, $S/D=0.5$ and 1.5 at $Re=1200$, were considered. The flow behaviour is well explained in a time series of stream function and vorticity contours. It is noted, however, that those computational data are compared with one flow visualization picture of Price et al. (2002), which is the only available PIV study in the literature on this flow configuration.

2. Experimental set-up and PIV measurements

The experiments were performed in a 12 m long recirculating open water channel with a rectangular cross-section of 0.3 m (W) × 0.45 m (H). A large settling tank and a 6:1 contraction precede the channel flume. All the side walls and the bed in the test-section were made of smooth glass. The slope of the channel bottom was adjusted prior to inserting any cylinder, such that a fully developed (i.e. zero-pressure-gradient) wall boundary layer was achieved in the test-section. During the experiments, the flow rate was maintained at 5.50 ± 0.02 L/s, and the water depth was maintained at about 100 mm in the test-section. As shown in Fig. 1, a cylinder with the diameter $D = 25$ mm was mounted horizontally and adjusted to the desired height (S) above the bottom wall. For the present investigation, S was set at 2.5, 5, 7.5, 10, 15, 20 and 25 mm, thus yielding the gap ratios (S/D) of 0.1, 0.2, 0.3, 0.4, 0.6, 0.8 and 1.0, respectively. The span (W) of the cylinder is 300 mm, and the aspect ratio of the cylinder span to its diameter (W/D) is 12. This aspect ratio of the experimental model is considered large enough to ensure a 2-D flow in the central region of the near wake. The origin of the coordinate system is set at the intersection between the cylinder base face and the channel bottom wall in the mid-plane of the channel. The coordinates x and y denote the streamwise and vertical directions, respectively.

Measurements were conducted using a PIV system (LaVision model). Based on a compromise between the requirements of recording a large field of view and resolving detailed flow structures, the viewing area of the PIV measurements was chosen at 75 × 75 mm (i.e. $3D \times 3D$) in the $x-y$ plane. For each case, two sets of PIV measurements were performed, covering two adjacent regions downstream of the cylinder, i.e. region I ($0 < x/D < 3$) and region II ($3 < x/D < 6$), as shown in Fig. 1. A Quantel System double cavity Nd:YAG laser (power ~120 mJ per pulse, duration ~5 ns) was used to illuminate the flow field. The particle images were recorded using an 8-bit charge-coupled device (CCD) camera, which has a resolution of 1024 × 1008 pixels and a frame rate of 15 Hz. Spherical® 110P8 hollow glass spheres (with a mean diameter of 13 μm and specific density of 1.1) from Potters Industries were seeded in the flow as the tracer particles, which offered good traceability and scattering efficiency. Considerable care was taken to ensure the high quality of the particle images, as the measurement uncertainty ultimately depends on that of the particle displacement calculated from the images.

The particle displacement was calculated using the cross-correlation algorithm with the standard Gaussian sub-pixel fit (Adrian, 1991) structured as an iterative multi-grid method (Scarano and Riethmuller, 1999). The processing procedure included two passes, starting with a grid size of 64 × 64 pixels, stepping down to 32 × 32 pixels overlapping by 50%. This interrogation and evaluation procedure yielded approximately 4000 velocity vectors (u, v) for each image pair. For most of the measurements, the field of view is 75 mm × 75 mm, therefore the spatial resolution for the present setup is about 1.2 mm × 1.2 mm (i.e. $0.048D \times 0.048D$). Then a range validation and a moving filter were used to reject erroneous vectors. For this purpose, a field of 3 × 3 vector neighbourhood was defined and the mean value and standard deviation were calculated. The central vector that has a value exceeding the mean value by three times the standard

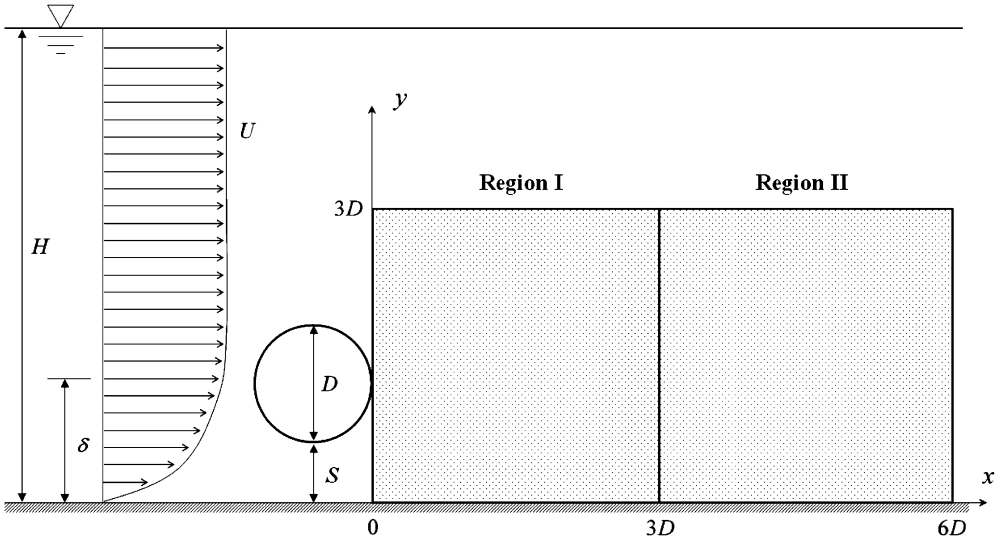

Fig. 1. Schematic diagram of the experimental setup and coordinate system.

deviation was deleted. For each experimental condition, a total of 360 samples were acquired at the frequency of 15 Hz (i.e. 24 s recordings), with the time delay between the double pulses at 700 μs.

Other parameters, including the particle image size (about 3 pixels) and seeding densities (about 30 particles/mm^2), were optimized to ensure valid detection of correlation peak. All the above settings satisfied the criteria proposed by Raffel et al. (1998). The uncertainty in the particle displacement was about 0.1 pixels. Detailed uncertainty analysis was given by Forliti et al. (2000) and Hyun et al. (2003), among others. Normalizing this uncertainty with the mean displacement of the particles in the free stream (4 pixels) yielded a relative error about 2.5% in the instantaneous velocities (u and v). Based on the velocity vector distribution, the spanwise vorticity ($\omega_z = \Delta v/\Delta x - \Delta u/\Delta y$) was calculated using the least operations extrapolation scheme, which is suitable for processing PIV data (Raffel et al., 1998). The uncertainty in ω_z was 10%. In the present study, the statistical characteristics of the flow (including the mean velocities U and V, and the Reynolds stress $-\overline{u'v'}$) were obtained by ensemble averaging of the 360 instantaneous fields. Following the procedure in Scarano and Riethmuller (1999) for the accuracy analysis due to finite number of PIV samples, the uncertainty in U and V in the present experiment was estimated to be 5%, and that in $-\overline{u'v'}$ was 10%.

To interpret the vortical structures in a more confident level, a combination of various vortex identification methods has been applied to the instantaneous velocity fields. According to the definition by Robinson (1991) for vortex identification (which has often been applied to PIV measurements in the past), a vortex exists when instantaneous streamlines mapped onto a plane normal to the vortex core exhibit a roughly circular or spiral pattern, in a reference frame that moves with the vortex (i.e. Galilean decomposition). However, the vortical structures may travel at different speeds, due to the fact that several different shear layers (e.g. the two shear layers from the top and down sides of the cylinder, and the wall boundary layer) exist in this flow configuration. Thus, the vorticity, which ensures frame independence, is calculated to help in interpreting the vortices. However, the vorticity may fail in identifying vortices, due to its inability to discriminate between shearing and swirling motions. A strong shear layer, like the wall boundary layer in this flow configuration, is associated with high vorticity but is not a vortex. For this purpose, the λ_2 criterion proposed by Jeong and Hussain (1995) is used, where λ_2 is the discriminant for complex eigenvalues. In a swirling region, λ_2 is large and negative; in a shearing region, on the contrary, it is positive. For 2-D velocity vectors, λ_2 is written as (Vollmers, 2001)

$$\lambda_2 = \left(\frac{\partial u}{\partial x} + \frac{\partial v}{\partial y}\right)^2 - 4\left(\frac{\partial u}{\partial x}\cdot\frac{\partial v}{\partial y} - \frac{\partial u}{\partial y}\cdot\frac{\partial v}{\partial x}\right).$$

More discussion on λ_2 is given in Wang and Tan (2007). In the present study, three different methods, i.e. Galilean decomposition of velocity vectors, calculation of ω_z and λ_2, are used.

The fully developed boundary layer over a smooth bed (i.e. in the absence of the cylinder) was carefully examined by 2-D LDV measurements (laser Doppler velocitmery, Dantec model). For this case, the free stream velocity U_e is 0.36 m/s and the boundary layer thickness δ is $0.4D$. The momentum thickness is calculated using $\theta = \int_0^\infty (U/U_e)[1-(U/U_e)]\,dy$. The calculated shape factor is $H = 1.33$, confirming that the incident boundary layer is fully developed. A summary of the parameters is given in Table 2.

PIV measurements were conducted on the fully developed boundary layer. In order to resolve the near-wall velocity profiles, an additional set of measurements was made by zooming in the PIV camera to record a 30 mm × 30 mm region with a spatial resolution of 0.5 mm. Fig. 2(a) shows the profile of the normalized mean velocity ($U^+ \equiv U/u_\tau$), which is measured by PIV, against the normalized vertical distance ($y^+ \equiv y u_\tau/v$), where $v = 8.94 \times 10^{-7}$ m^2/s is the kinematic viscosity of water at 25 °C. Also shown in the figure are the theoretical functions of the wall, including the linear relationship $U^+ = y^+$ and the log–law relationship (Adrian et al., 2000):

$$U^+ = \frac{1}{\kappa}\ln(y^+) + A,$$

Table 2
Statistics of the boundary layer over the smooth wall

Free stream velocity U_e (m/s)	0.36
Friction velocity u_τ (m/s)	0.00187
Boundary layer thickness δ (mm)	10
Displacement thickness δ^* (mm)	1.37
Momentum thickness θ (mm)	1.02
Shape factor H ($= \delta^*/\theta$)	1.33

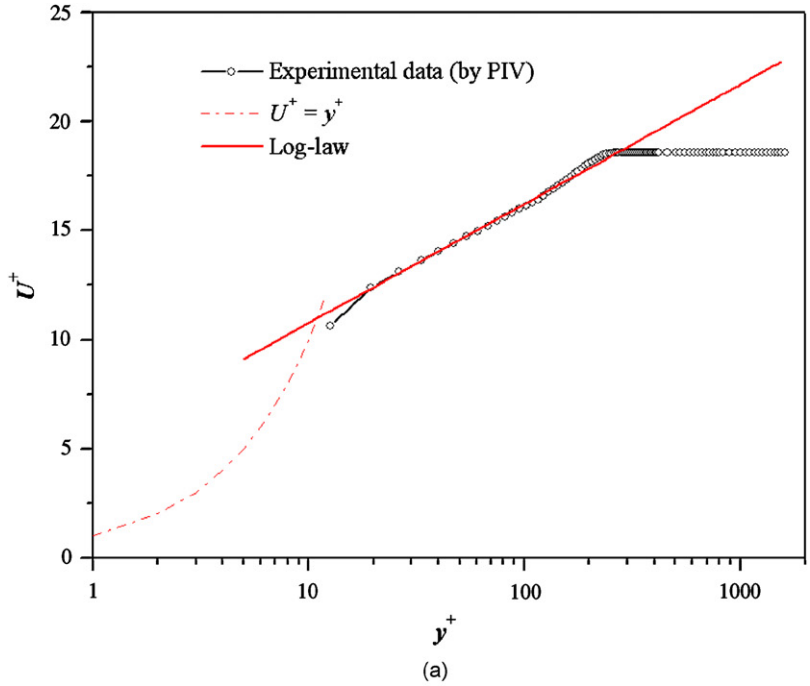

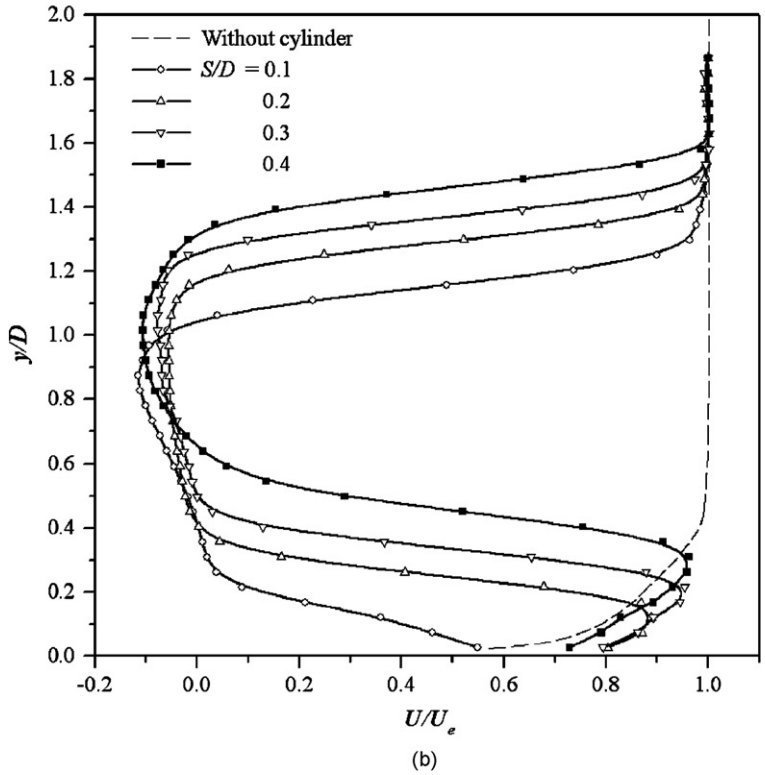

Fig. 2. (a) Mean velocity profiles over smooth bed (no-cylinder case), scaled and plotted with the inner variable u_τ; (b) profiles of U/U_e at $x = 0$ for $S/D = 0.1$–0.4, together with that for the smooth bed (no-cylinder case).

where the von Kármán constant $\kappa = 0.41$ and the integral constant $A = 5.29$. The data show good agreement with the log–law in the range $20 < y^+ < 200$, indicating that the flow is fully developed in the test-section. In the presence of the cylinder, U_e became higher at about 0.42 m/s due to the blockage effect as compared to the no-cylinder case. The Reynolds number is $\mathrm{Re} = U_e D/v \approx 1.2 \times 10^4$. Fig. 2(b) shows the profiles of U/U_e at $x = 0$ for $S/D = 0.1$, 0.2, 0.3 and 0.4. The dashed line represents that of the no-cylinder case, with a boundary layer thickness $\delta = 0.4D$. Even for the smallest gap ratio ($S/D = 0.1$), a jet-like flow, with the largest mean velocity of about $0.5U_e$ in the gap, has been observed. The largest velocity of the gap flow increases with increasing S/D, reaching $0.95U_e$, $0.97U_e$, and $0.98U_e$ for $S/D = 0.2$, 0.3 and 0.4, respectively.

3. Results and discussion

3.1. Ensemble-averaged flow fields

The mean flow quantities were obtained by ensemble averaging the 360 instantaneous velocity vector fields for each experimental condition. Fig. 3(a)–(d) shows the mean velocity vector (U, V) plot in region I ($0 < x/D < 3$) for $S/D = 0.1$, 0.2, 0.3 and 0.4, respectively. Streamlines are included in these figures to highlight the flow structure. It is clearly seen that the presence of the wall significantly affects the (U, V) distributions particularly for small values of gap ratio.

For $S/D = 0.1$ (Fig. 3(a)), since the gap flow is considerably weaker than the free stream, the flow structure is similar to either that of the cylinder touching the wall (i.e. $S/D = 0$, not shown here), or that of a backward-facing step flow. Two recirculation regions, entrapped by the shear layers separated from both sides of the cylinder, can be identified: the primary, clockwise recirculation region extends from the upper side of the cylinder until the reattachment; the secondary, anticlockwise one is located immediately downstream of the lower half of the cylinder. The mean reattachment point occurs at about $4.8D$ (determined by PIV measurement in region II, $3 < x/D < 6$), whereas the secondary recirculation region ends up at about $1.4D$. For $S/D = 0.2$ (Fig. 3(b)), the two recirculation regions are also asymmetric about the cylinder centreline $y/D = S/D + 0.5$. The lower recirculation region is longer than the upper one, which is due to that straightening effect of the wall boundary layer. For larger gap ratios, namely $S/D = 0.3$ and 0.4 (Fig. 3(c) and (d)), the mean flow becomes reasonably symmetric. Another trend is that the streamwise length of the recirculation region decreases as S/D increases.

Fig. 4(a)–(d) is the contour plots of the normalized Reynolds stress $-\overline{u'v'}/U_e^2$ for $S/D = 0.1$, 0.2, 0.3 and 0.4, respectively. Results for larger gap ratios ($S/D > 0.4$) are essentially similar to that of $S/D = 0.4$, and thus are not shown herein. For $S/D = 0.1$ (Fig. 4(a)), the distributions of $-\overline{u'v'}/U_e^2$ are obviously asymmetric about the cylinder centreline $y/D = S/D + 0.5$: an elongated region with concentrated positive Reynolds stress occurs in the upper shear layer, whereas in the lower shear layer only low levels of negative Reynolds stress are evident. For $S/D = 0.2$ (Fig. 4(b)), the lower shear layer becomes stronger and the distributions of $-\overline{u'v'}/U_e^2$ become more symmetric about $y/D = S/D + 0.5$. For $S/D = 0.3$ (Fig. 4(c)) and 0.4 (Fig. 4(d)), besides the two large-scale clusters of $-\overline{u'v'}/U_e^2$, there are two additional small-scale clusters located immediately downstream of the cylinder base. This feature agrees with that reported in Dong et al. (2006) on a 2-D stand-alone circular cylinder at comparable Reynolds numbers (Re = 4000 and 10,000 in their study). As S/D increases from 0.1 to 0.4, the entire pattern of Reynolds stress has moved a substantial distance upstream to the cylinder base. For instance, the location of the peak Reynolds stress moves upstream with increasing S/D, from $x/D = 2.0$ for $S/D = 0.1$ to $x/D = 1.0$ for $S/D = 0.4$. The magnitude of the normalized Reynolds stress, $|-\overline{u'v'}/U_e^2|_{\max}$, increases from 0.025 for $S/D = 0.1$ to 0.06 for $S/D = 0.4$.

Fig. 5 shows the variation of the recirculation region length (L_r/D, where L_r is the streamwise distance of the location at which the mean velocity $U = 0$) and the Reynolds stress magnitude ($|-\overline{u'v'}/U_e^2|_{\max}$) with the gap ratio ($S/D$). While L_r decreases monotonically with the increase of S/D, a dramatic decrease of L_r is found over the range $0.1 \leqslant S/D \leqslant 0.4$. For $S/D \geqslant 0.6$, L_r remains essentially constant at $L_r/D \approx 1.0$, indicating that the influence of the wall is gradually diminishing. On the other hand, $|-\overline{u'v'}/U_e^2|_{\max}$ increases with increasing S/D, with a sharp increase over the range $0.1 \leqslant S/D \leqslant 0.4$. For $S/D \geqslant 0.6$, $|-\overline{u'v'}/U_e^2|_{\max}$ maintains at a constant value of about 0.065. In comparison, for the stand-alone cylinder in Dong et al. (2006), the corresponding values measured by PIV are $L_r/D \approx 0.85$ and $|-\overline{u'v'}/U_e^2|_{\max} \approx 0.15$ at Re = 10 000. The relatively larger value of L_r/D and smaller value of $|-\overline{u'v'}/U_e^2|_{\max}$ in the present study are reasonable, considering the straightening effect of the wall boundary layer. These observations of the mean velocity vector and Reynolds stress distributions suggest discernible differences in the instantaneous flow structure for different gap ratios, which are to be addressed in the next section.

3.2. Suppression or formation of vortex shedding in the instantaneous flow fields

Figs. 6–10 show a representative snapshot of the instantaneous flow field in region I for $S/D = 0.1$, 0.2, 0.3, 0.4 and 0.6, respectively. When selecting the images, attention was paid to match the instantaneous flow structure at a similar

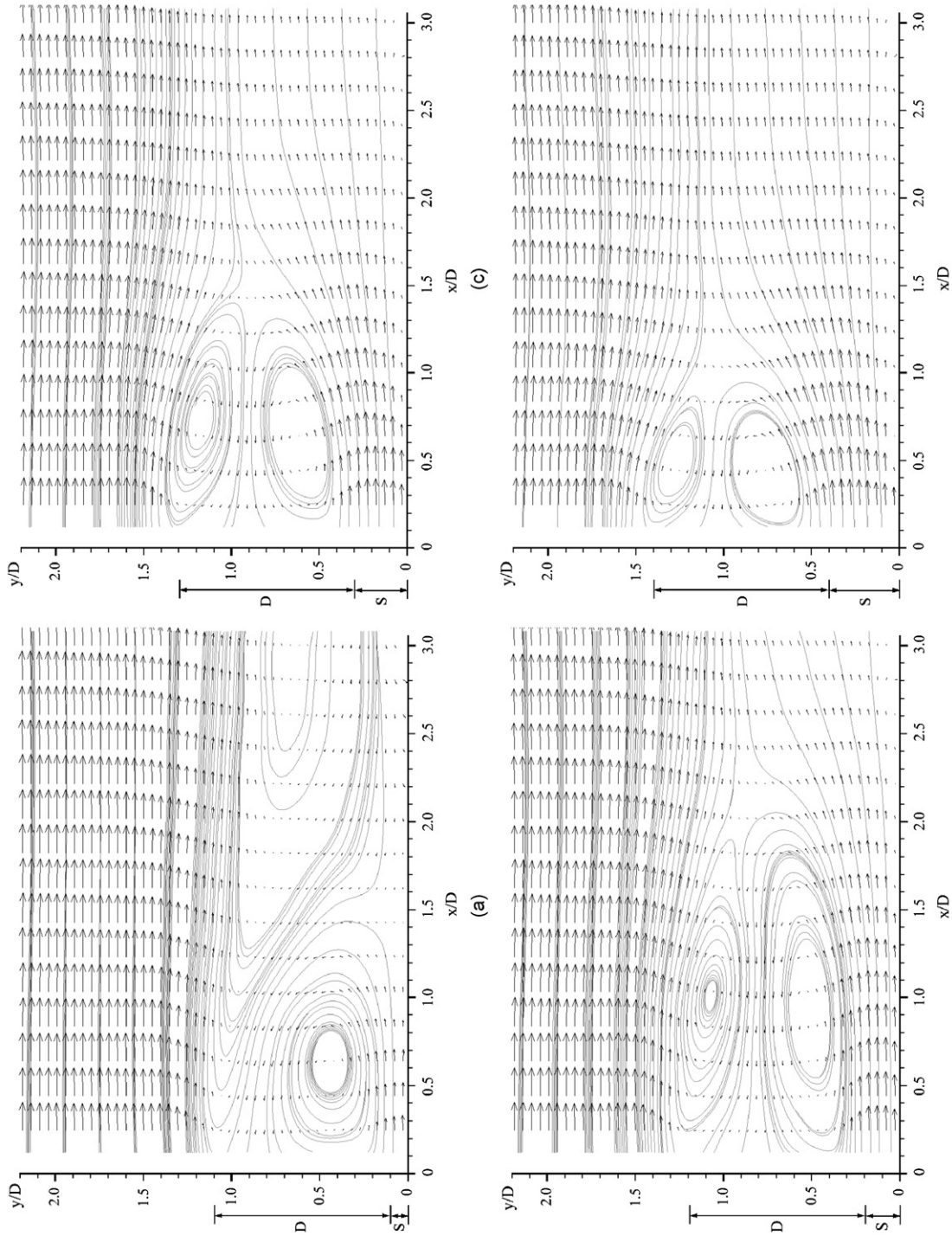

Fig. 3. Mean velocity vector (U, V) plot for: (a) $S/D = 0.1$, (b) 0.2, (c) 0.3, and (d) 0.4.

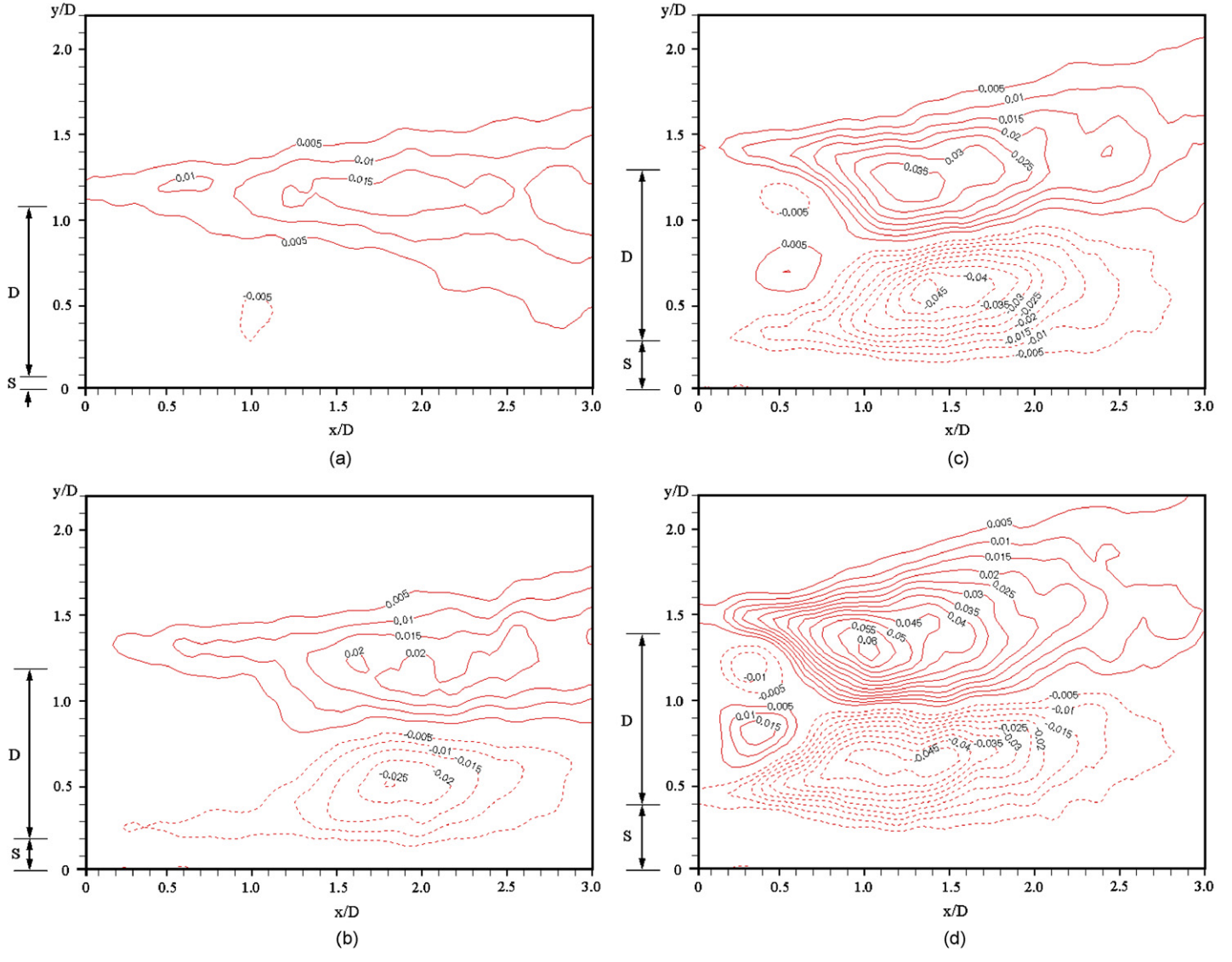

Fig. 4. Contour plot of the normalized Reynolds stress ($-\overline{u'v'}/U_c^2$) for: (a) $S/D = 0.1$, (b) 0.2, (c) 0.3, and (d) 0.4. Positive: solid lines, negative: dashed lines. Contour interval is 0.005.

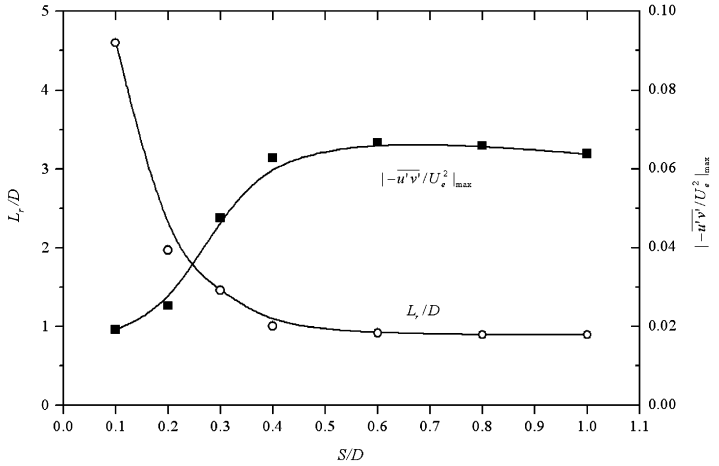

Fig. 5. Variation of L_r/D and $|-\overline{u'v'}/U_e^2|_{\max}$ versus S/D.

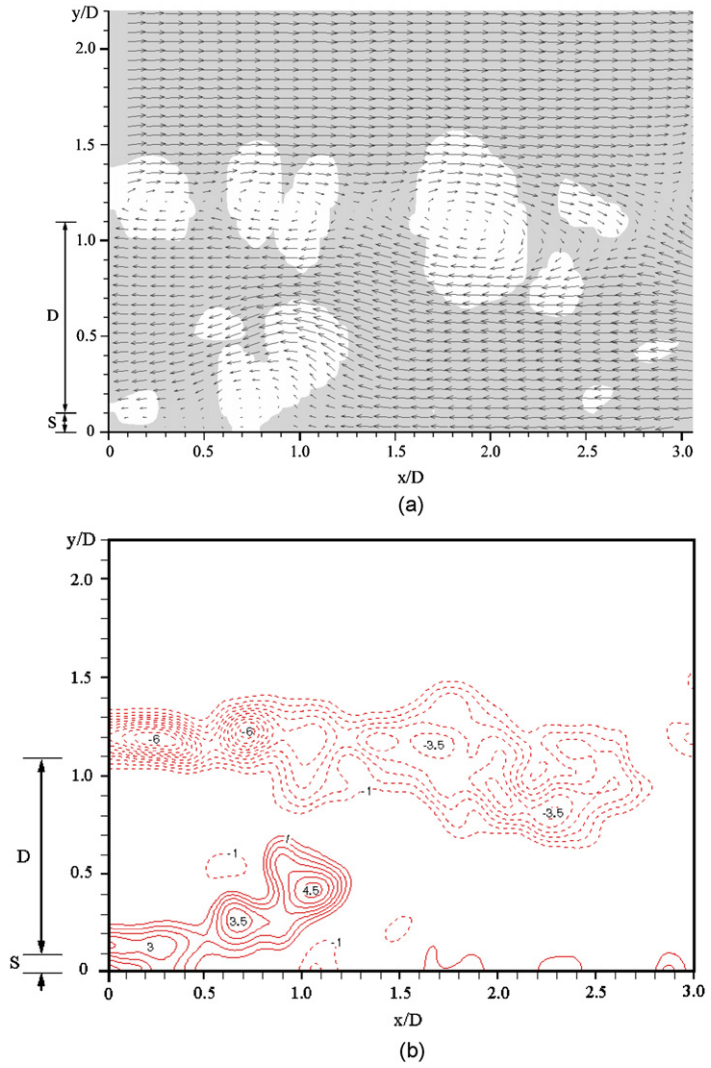

Fig. 6. A snapshot of the instantaneous flow field for $S/D = 0.1$: (a) the instantaneous velocity vector (u, v) plot (with reference to $0.41U_e$), superimposed with contours of swirling strength λ_2 (grey region: $\lambda_2 > 0$; white region: $\lambda_2 < 0$); (b) contour plot of the normalized spanwise vorticity $\omega_z D/U_e$.

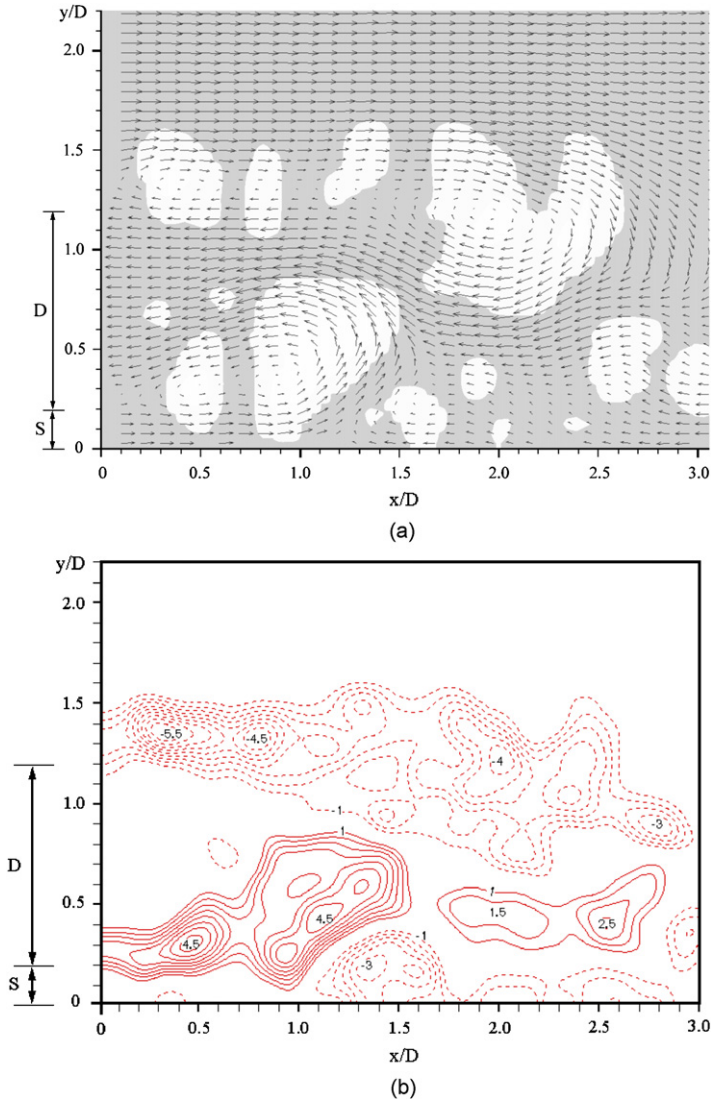

Fig. 7. A snapshot of the instantaneous flow field for $S/D = 0.2$. For caption, see Fig. 6.

phase of the cycle of large-scale vortex formation. Galilean decomposition was applied to the velocity vectors, where a fixed streamwise reference velocity equal to $U_{ref} = 0.5U_e$ was subtracted. Grey-sale contours of the calculated λ_2 are also superimposed in these figures, where white colours stand for regions of swirling ($\lambda_2 < 0$). It is shown that most regions of swirling ($\lambda_2 < 0$) match the vortices that are identified as circular pattern of velocity vectors. Figs. 6(b)–10(b) are the corresponding contour plots of spanwise vorticity (which is normalized as $\omega_z D/U_e$). The anticlockwise (positive) and clockwise (negative) vortices are represented by solid and dashed lines, respectively. As illustrated hereafter, the formation or suppression of vortex shedding is intimately associated with the coupling (or interaction) of the separated shear layers.

For $S/D = 0.1$ (Fig. 6), both shear layers develop as elongated chains of vortices. The lower shear layer is considerably weaker than the upper one, as indicated by the vorticity magnitude, $|\omega_z D/U_e|_{\max}$, of 4.5 versus 6.0. The vorticity-concentrated regions in Fig. 6(b) are mainly regions of swirling ($\lambda_2 < 0$) in Fig. 6(a), except in the very near-wall region (i.e. $y/D \approx 0$) and in the regions between adjacent vortices (e.g. saddle points in the velocity vectors) where pure shearing ($\lambda_2 > 0$) may occur. While the upper shear layer is the standard Kelvin–Helmholtz (K–H) roll-ups and extends over the field of view, the lower shear layer ends up at about $x/D = 1.2$, which thereafter dissipates due to the fluid viscosity. The flow structure for $S/D = 0.2$ (Fig. 7) is similar to that of $S/D = 0.1$. However, for this case, the gap flow is

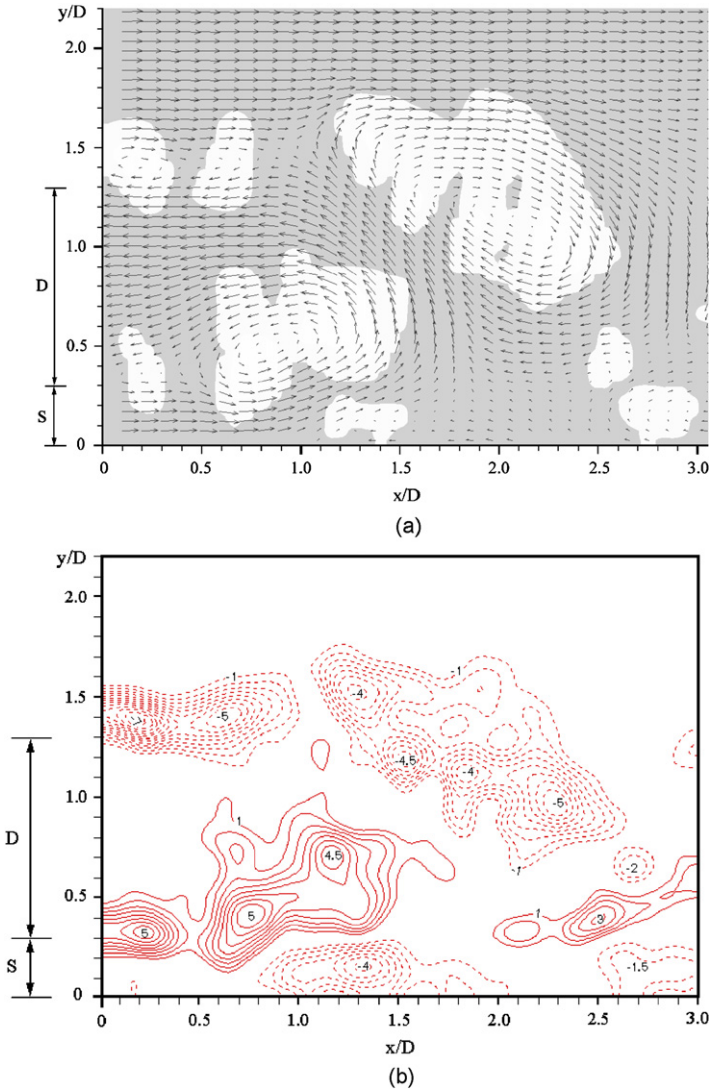

Fig. 8. A snapshot of the instantaneous flow field for $S/D = 0.3$. For caption, see Fig. 6.

stronger than that for $S/D = 0.1$, thus the lower shear layer extends further downstream distance of $x/D = 1.6$. The upper shear layer in Fig. 7 ($S/D = 0.2$), which was kept nearly horizontal in Fig. 6 ($S/D = 0.1$), bends downward and becomes more diffused in the vertical direction, which is likely attributed to the inducement of the stronger lower shear layer for this case. However, for these two gap ratios, $S/D = 0.1$ and 0.2, there is no mutual coupling between the two shear layers. Although the lower shear layer exhibits an upward deflection at the right end before it dissipates, it is not sufficient to be shed as discrete vortex. This is contrary to the suggestions of Grass et al. (1984) and Taniguchi and Miyakoshi (1990) that the concentrated vorticity from the lower side of the cylinder is cancelled by the opposite vorticity at the wall for small values of S/D.

For $S/D = 0.3$ (Fig. 8), the lower shear layer is still both smaller in size and weaker in magnitude as compared to the upper one; however, both layers begin to curl up and periodically shed from the cylinder, so that the Kármán-like vortex shedding is observed for this gap ratio. Fig. 8 is a snapshot where a clockwise vortex is just shed on the upper side and an anticlockwise vortex is being formed at the lower side. These well-defined vortices are evident as distinct regions of swirling ($\lambda_2 < 0$) in Fig. 8(a) and concentrated vorticity in Fig. 8(b), with a length scale about the cylinder diameter (D). As S/D increases to 0.4 (Fig. 9) and 0.6 (Fig. 10), the coupling between the two shear layers becomes stronger. With increasing gap ratio, the deflection curvature of the two shear layers becomes greater, so that the vortex shedding moves

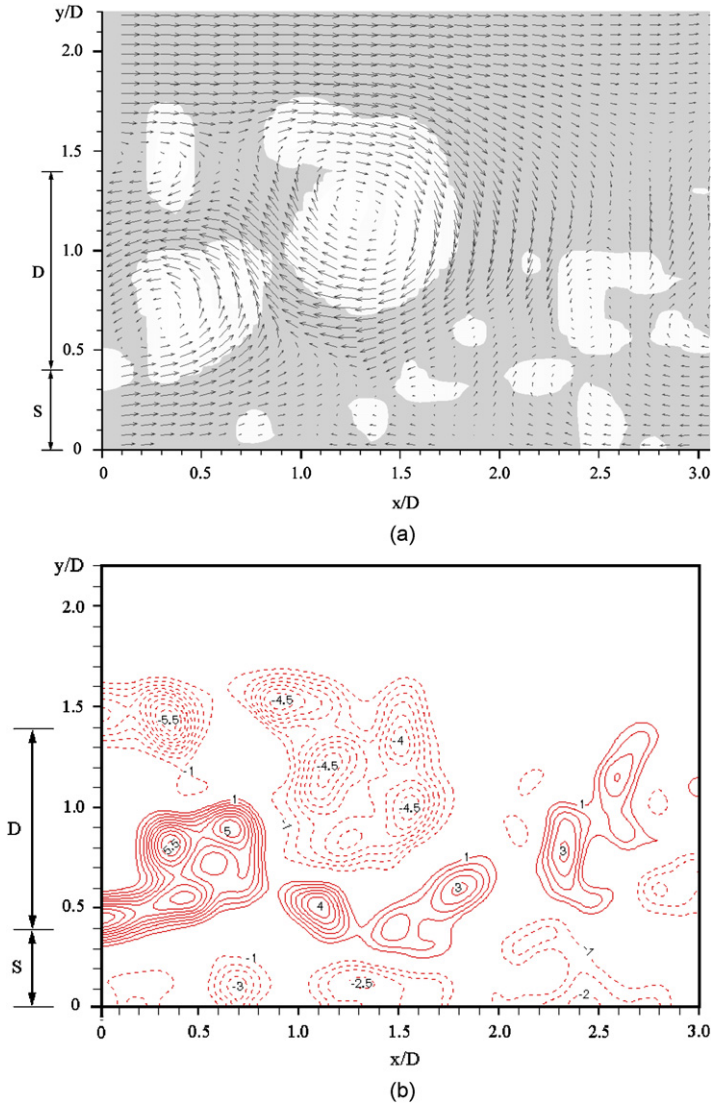

Fig. 9. A snapshot of the instantaneous flow field for $S/D = 0.4$. For caption, see Fig. 6.

towards the cylinder base. The coupling (or interaction) between the two shear layers is believed to account for the sharp decrease of L_r/D and the sharp increase of $|-\overline{u'v'}/U_e^2|_{\max}$ over the range $S/D = 0.1$–0.4, as shown in Fig. 5.

For $S/D = 0.3$, 0.4 and 0.6 (Figs. 8–10), although vortex shedding is periodic, the influence of the wall is a fairly strong, causing the flow to be asymmetric about the cylinder centreline $y/D = S/D + 0.5$. As compared to the upper clockwise vortices, the lower anticlockwise vortices appear to be smaller and develop as vertically elongated chains of vorticity. The flow characteristics may explain why the mean lift coefficient shown in Lei et al. (1999) is not zero for cases of small S/D. The flow asymmetry gradually decreases with increasing S/D. For $S/D \geqslant 0.8$ (not shown for brevity), the influence of the wall can be neglected and the symmetry of the two shear layers is satisfied.

The effects of S/D on the wall boundary layer can be appreciated by inspecting the flow patterns in the near-wall region. For $S/D = 0.1$ and 0.2 (Figs. 6 and 7), the gap flow keeps attached to the wall until at $x/D \approx 1.2$ and 1.6, respectively, wherein a flow separation occurs due to the upward deflection of lower shear layer. This flow separation remains basically steady over time, since the lower shear layer is not shed as discrete vortices. For $S/D = 0.3$, 0.4 and 0.6 (Figs. 8–10), in contrast, the wake flow is characterized by the periodic Kármán-like vortex shedding. The anticlockwise vortices shed from the lower side of the cylinder clearly destabilize the wall boundary layer due to the vortex-induced adverse pressure gradient. Each anticlockwise vortex is likely to be accompanied by a secondary, clockwise vortex in the

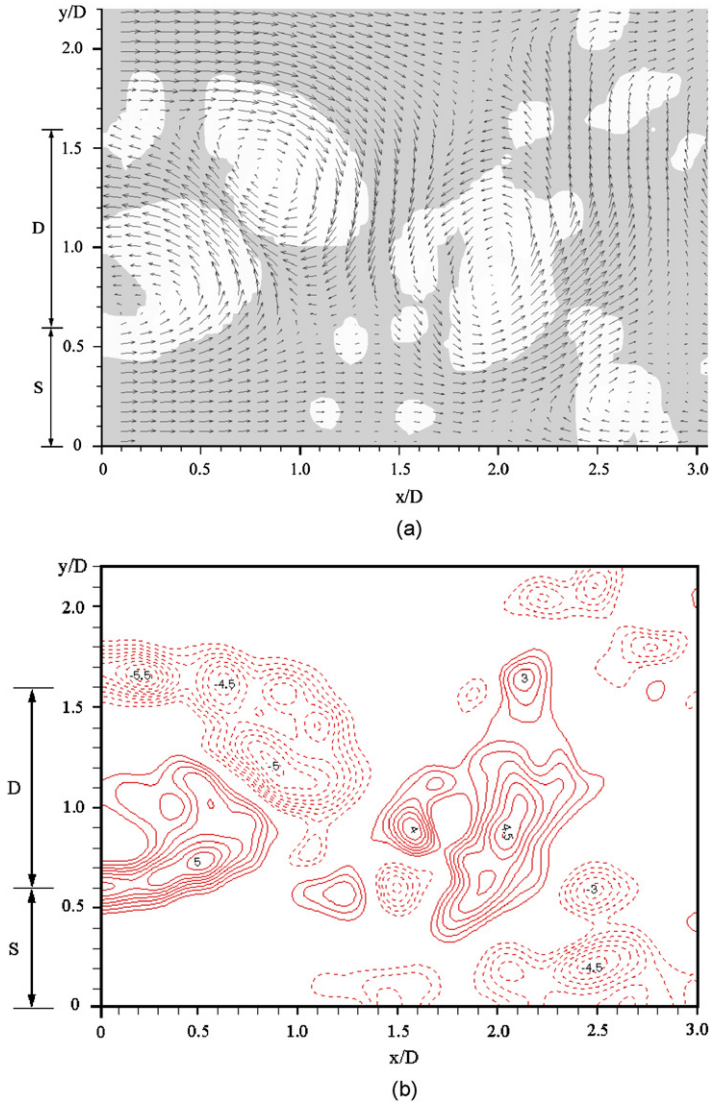

Fig. 10. A snapshot of the instantaneous flow field for $S/D = 0.6$. For caption, see Fig. 6.

near-wall region. As a result, the flow near that region detaches from the wall and ejects upward, which can be observed in the velocity vectors. The vortex-induced instability is predicted by the vortex dynamic computation in Dipankar and Sengupta (2005). A similar phenomenon is reported by Price et al. (2002): that for $0.125 < S/D < 0.5$ there is a pairing between the lower shear layer and the wall boundary layer. For large gap ratios $S/D \geqslant 0.8$, on the other hand, the induced vortices in the near wall region drop to an almost negligible level.

Based on the above results, three different flow regimes can be classified as a function of S/D. (i) In the far wall regime ($S/D \geqslant 0.8$), the flow and shedding characteristics are similar to a stand-alone cylinder (i.e. the no-wall case). (ii) In the near wall regime ($0.3 \leqslant S/D \leqslant 0.6$), vortex shedding is still evident, but the wall effect is considerable: the upper and lower shear layers are asymmetric to each other; and there is strong pairing between the lower shear layer and the wall boundary layer. (iii) In the suppressed regime ($S/D \leqslant 0.2$), the periodic vortex shedding is suppressed.

3.3. Shedding frequency, vortex motion and downstream variation of vortex characteristics

Spectral analysis was applied to the obtained velocity data to illustrate the periodic nature of the flow within the measurement range from $f = 0$ to 7.5 Hz (which is the half of the sampling frequency of 15 Hz). Fig. 11 shows the power

spectral density of the vertical velocity (v) at the streamwise position $x/D = 1.5$, where the periodic vortex shedding can be easily detected according to the instantaneous flow fields shown above. Results at three vertical locations, i.e. L, U and M, respectively for $y/D = S/D$ (corresponding to the lower shear layer), $S/D + 1.0$ (the upper shear layer) and $S/D + 0.5$ (the cylinder centreline, which is the middle point between L and U), are given. The figures are plotted with different vertical scales so that the peaks can be seen clearly. For $S/D = 0.1$ (Fig. 11(a)), there is no obvious peak over the measurement range. For $S/D = 0.2$–0.8 (Fig. 11(b)–(f)), there is always a predominant peak at about $f = 3.1 \pm 0.1$ Hz in the spectra at locations M and U, which is virtually independent of the gap ratio (S/D). The spectral peak at location L is less evident than that at either M or U particularly for small gap ratios ($S/D \leqslant 0.4$). However, it becomes visible for $S/D \geqslant 0.6$, at the same value of $f = 3.1 \pm 0.1$ Hz. This gives a Strouhal number of $\mathrm{St} = fD/U_e \approx 0.19$, which is in agreement with that of $\mathrm{St} \approx 0.2$ reported by most previous studies. For cases of $S/D \geqslant 0.3$, this frequency is apparently that of the periodic vortex shedding. The peak value increases monotonically with increasing S/D: as exemplified from that of location M, it increases from 3.8×10^{-5} for $S/D = 0.3$ (Fig. 11(c)), to 7.0×10^{-5} for $S/D = 0.8$ (Fig. 11(f)). This indicates that the strength of vortex shedding becomes stronger as the gap ratio increases (similar trend is inferred from the instantaneous flow fields). The spectral peak for $S/D = 0.2$ (with a peak value of 2.5×10^{-5}) is, however, a surprise because there is no vortex shedding according to Fig. 6. This will be illustrated in time series of the instantaneous flow fields as follows.

A sequence of four instantaneous flow fields, following the snapshot in Fig. 9, is shown in Fig. 12(a)–(d) for the case of $S/D = 0.4$. This sequence represents approximately a vortex shedding cycle and the time interval between two consecutive snapshots is 1/15 s. At $t = 0$ (Fig. 9), a large, negative vortex (labelled as A) is to be shed from the upper side, with a small, positive vortex (labelled as B) being formed below. Consequently, as vortex A convects downstream, vortex B continues to grow in size at $t = 1/15$ s (Fig. 12(a)) and 2/15 s (Fig. 12(b)), and finally shed as a discrete vortex at $t = 3/15$ s (Fig. 12(c)) and 4/15 s (Fig. 12(d)). Note that towards the end of the cycle (Fig. 12(d)), a new negative vortex (labelled as A′) is to be shed from the upper side, initiating another cycle of vortex shedding. This time series of the instantaneous flow field shows how the two shear layers alternately roll-up, forming the vortex shedding. The vortex shedding is periodic in time but it occurs obliquely in space. While vortex A is nearly circular in shape, vortex B is in the form of vertically elongated (or even sometimes broken) concentrations, with their trajectories moving away from the wall. It is also evident that vortex shedding destabilizes the wall boundary layer, causing it to separate in the form of a negative vortex (labelled as C in the figures), which periodically convect downstream at the same frequency as that of vortex shedding. The asymmetric vortex shedding from the two sides of the cylinder and the vortex-induced separation in the near-wall region have been predicted numerically by Dipankar and Sengupta (2005) for the gap ratio $S/D = 0.5$.

To explain the spectral peak for $S/D = 0.2$, two consecutive snapshots of the instantaneous flow field, following that of Fig. 7, are shown in Fig. 13(a) and (b). At $t = 0$ (Fig. 7), the right end of the upper shear layer (about $1.5 < x/D < 2.5$) exhibits as a region of both swirling ($\lambda_2 < 0$) and somewhat loosely concentrated negative vorticity ($\omega_z < 0$), although it is not as distinct as that of a discrete vortex. This region continues to grow and moves further downstream at the subsequent instant $t = 1/15$ s (Fig. 13(a)), and finally is detached as a discrete vortex (labelled as D) at $t = 2/15$ s (Fig. 13(b)). Thereafter, the cut-off upper shear layer resumes to grow in size, repeating the process as described above. This process in the upper shear layer is essentially cyclical, resulting in the spectral peak shown in Fig. 11(b). The lower shear layer, on the other hand, basically remains steady (or frozen in time) and cannot be shed as a vortex. Therefore, the spectral peak in the velocity data for $S/D = 0.2$ should not be interpreted as vortex shedding. This observation also illustrates that cautions should be paid to interpret vortex shedding behaviour based on spectral analysis of velocity data.

A summary of the corresponding Strouhal number data for the present study and several previous studies is given in Fig. 14. The present data agree reasonably well with most of those reported in the literature. However, it is noted that the reported values in Price et al. (2002) at $\mathrm{Re} = 1900$ can be high as about 0.4 for $S/D \leqslant 0.25$. The extraordinarily high values of St were suggested to be associated with a periodicity in the upper shear layer rather than as opposed to regular vortex shedding (Price et al., 2002). The present data, on the other hand, indicate that the Strouhal number is insensitive to S/D, remaining constant at about 0.19 over the range $0.2 \leqslant S/D \leqslant 1.0$.

Moreover, to illustrate the subsequent evolution of the vortices after they are shed, PIV measurements are taken in region II ($3 < x/D < 6$). Fig. 15(a) shows the trajectory of the centre of a vortex shed from the upper side of the cylinder for the case of $S/D = 0.2$, based on five consecutive snapshots of the instantaneous flow field (the time interval is 1/15 s). The third and fourth snapshots, i.e. ③ and ④, are shown in Fig. 16(a) and (b), respectively. Since the vortex is very distinct, its centre is defined as the local extrema of the vorticity. As shown in Fig. 15(a), the trajectory of the vortex centre remains horizontal at $y/D \approx 1$, although the vortex moves slightly towards the wall in the range $3 < x/D < 4$ and thereafter slightly upward away from the wall. The streamwise convection velocity U_c, as can be determined by differentiating the streamwise positions of the vortex, keeps constant about $0.5U_e$ in this region. The convection velocity matches that of the reference frame for Galilean decomposition, explaining why the circular pattern of velocity vectors

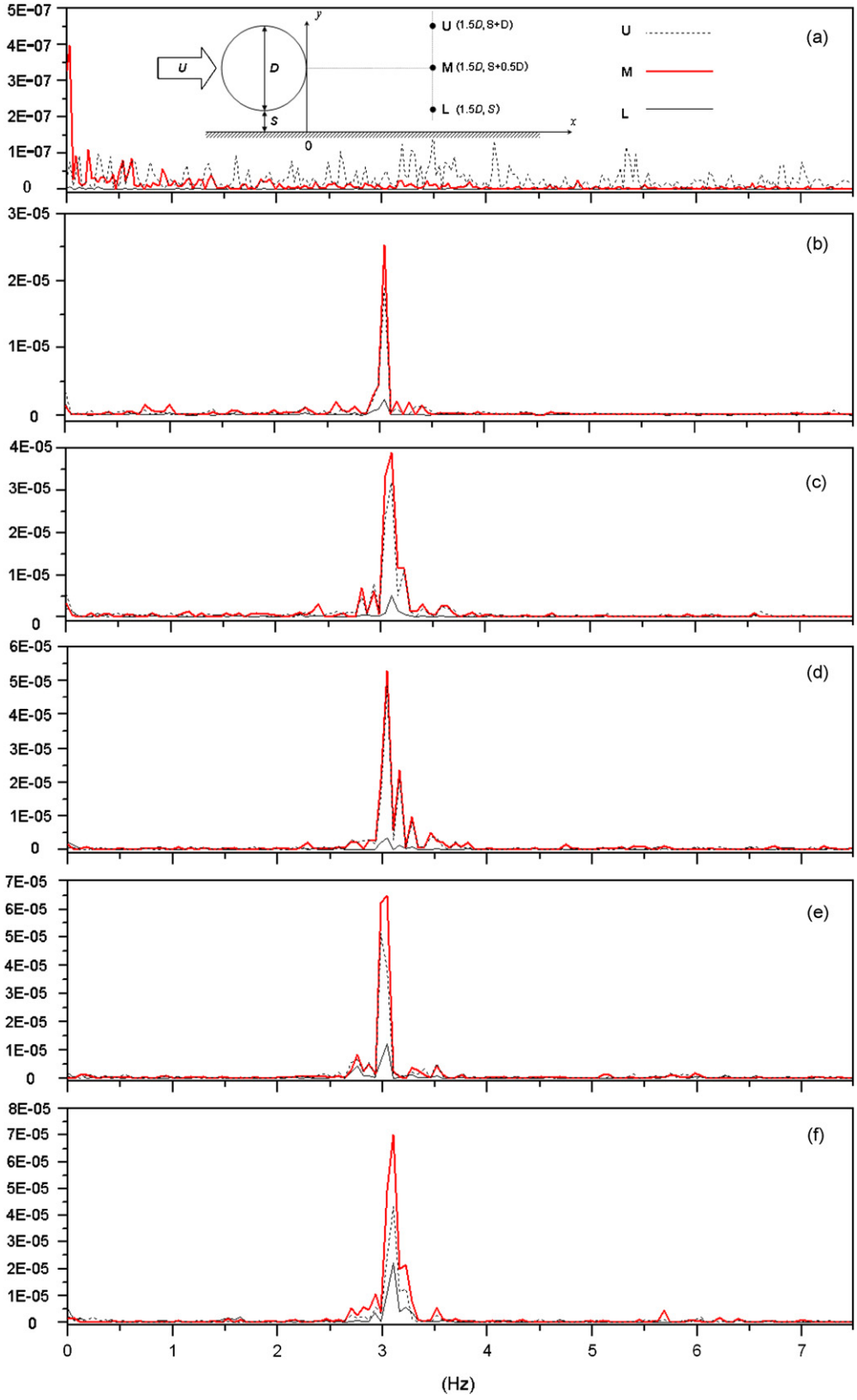

Fig. 11. Power spectral density of v for: (a) $S/D = 0.1$, (b) 0.2, (c) 0.3, (d) 0.4, (e) 0.6, and (f) 0.8.

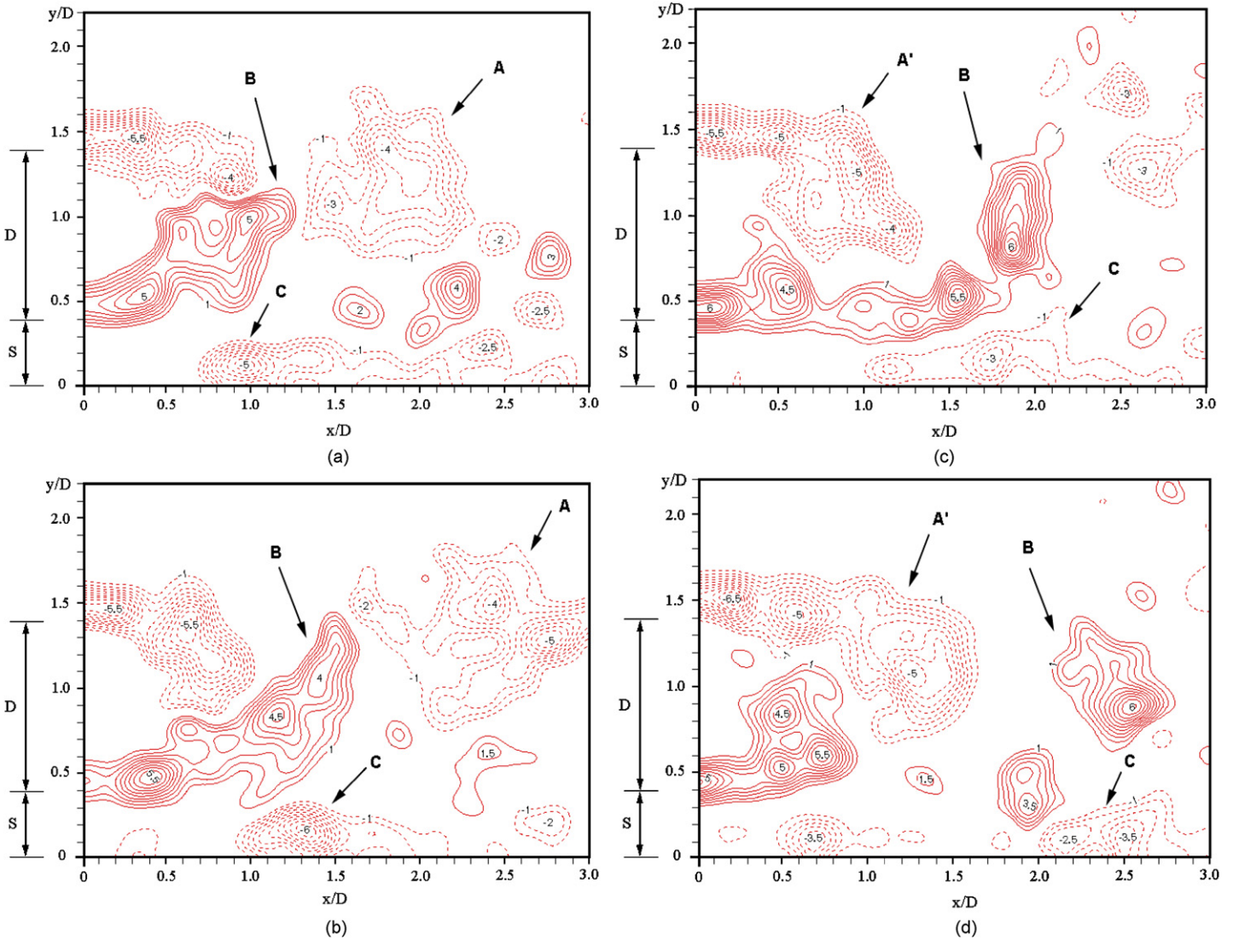

Fig. 12. A time series of contour plots of $\omega_z D/U_e$ for $S/D = 0.4$: (a) $t = 1/15$ s, (b) 2/15 s, (c) 3/15 s, and (d) 4/15 s.

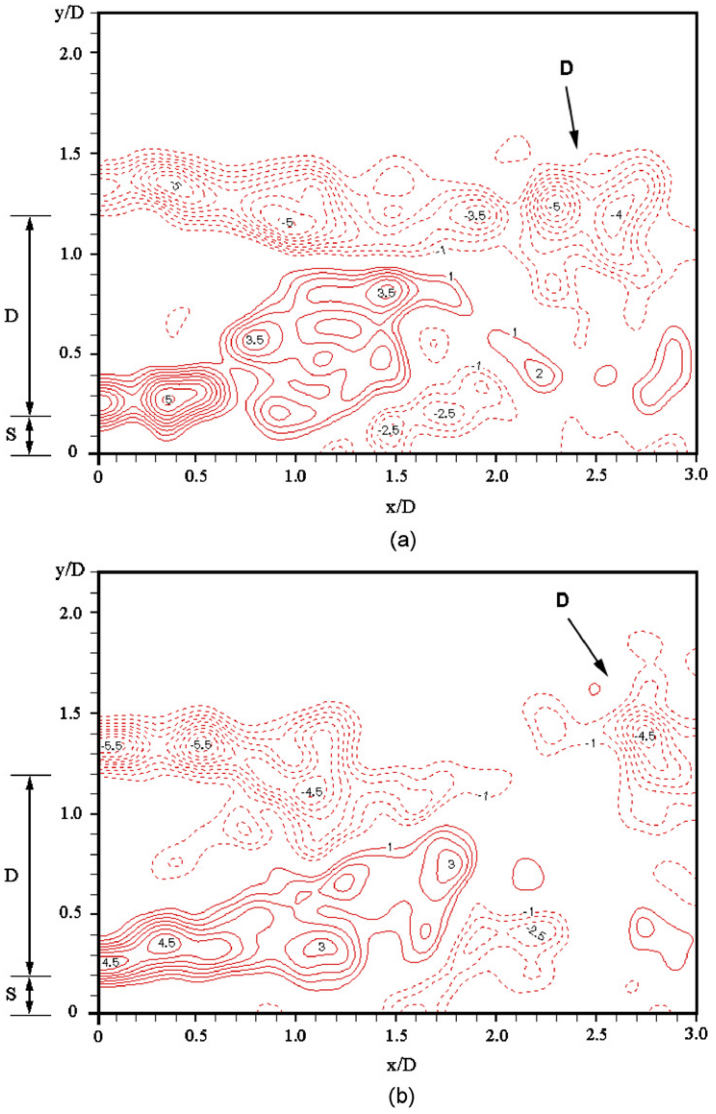

Fig. 13. A time series of contour plots of $\omega_z D/U_e$ for $S/D = 0.2$: (a) $t = 1/15$ s and (b) 2/15 s.

always coincides closely with vorticity-concentrated region in these images. It is slower than the reported values in Cantwell and Coles (1983) on a stand-alone cylinder that $U_c = 0.83U_e$ in the range $x/D<3$ and $U_c = 0.55U_e$ in the range $x/D>4$. The difference in convection velocity is likely attributed to the confinement effect due to the wall proximity.

The shape of the shed vortex is also evident in Fig. 16, which is nearly circular but slightly elongated in the streamwise direction. Since the vortex is easily identifiable as distinct regions of vortictiy, an attempt is made to quantify its strength in terms of circulation (Γ). For this purpose, the boundary of the vortex is defined as regions of swirling ($\lambda_2<0$). After the boundary is determined, Γ is calculated from area integration of vorticity,

$$\Gamma = \int\int_A \omega_z \, \mathrm{d}x \, \mathrm{d}y.$$

Fig. 15(b) shows that the circulation keeps nearly constant at $|\Gamma/(DU_e)| \approx 1.0$ as the vortex travels downstream within the field of view, but at the farthest locations ($x/D>5$) it may decline slightly. This trend is in accordance with the observation of Cantwell and Coles (1983) on the shed vortex from a stand-alone cylinder that the circulation slowly decays with an average rate of decay $\approx 8\%$ per diameter of travel over the range $x/D \approx 4$–8.

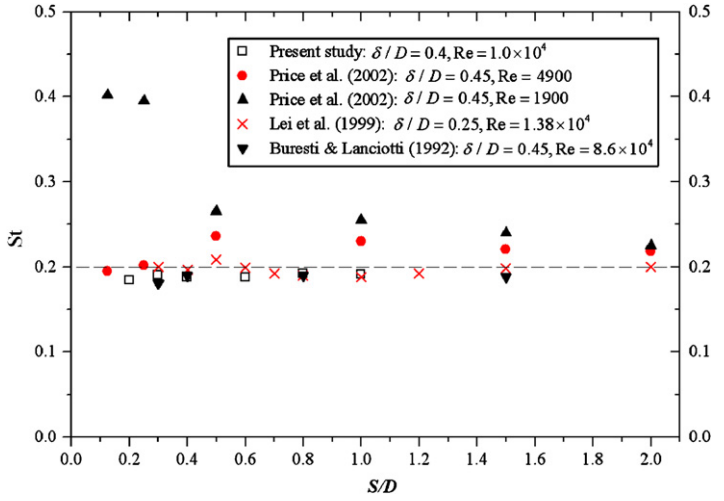

Fig. 14. Variation of Strouhal number (St) versus gap ratio (S/D).

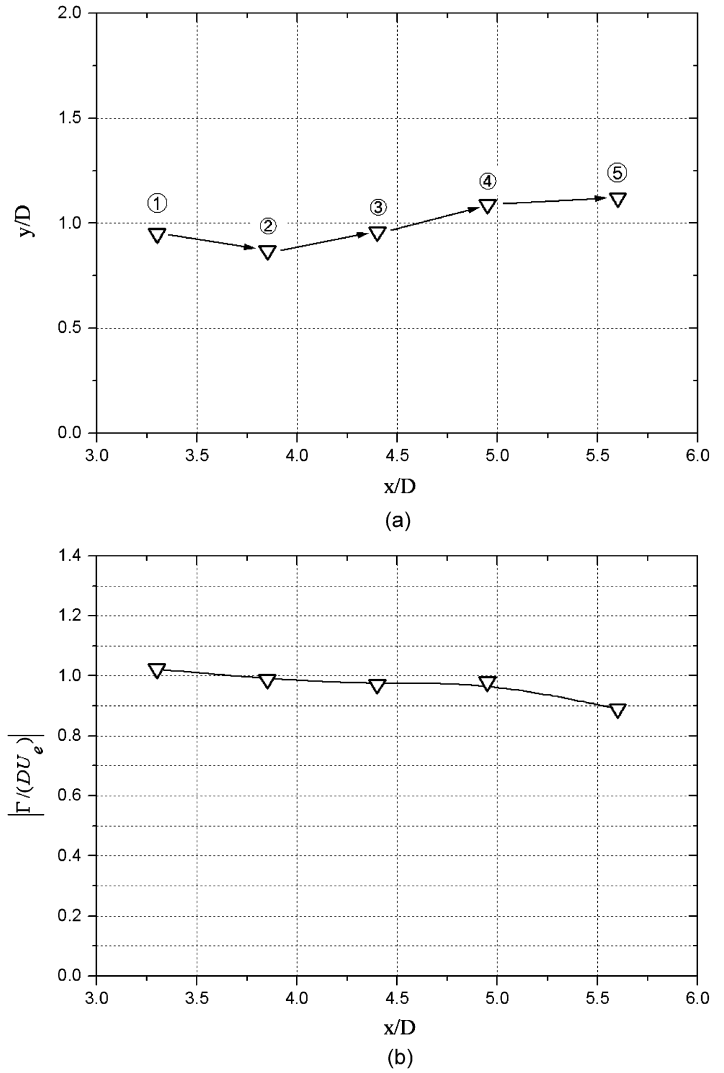

Fig. 15. Evolution of the shed discrete vortices for $S/D = 0.2$ in region II ($x/D = 3$–6): (a) trajectory and (b) circulation $|\Gamma/(DU_e)|$.

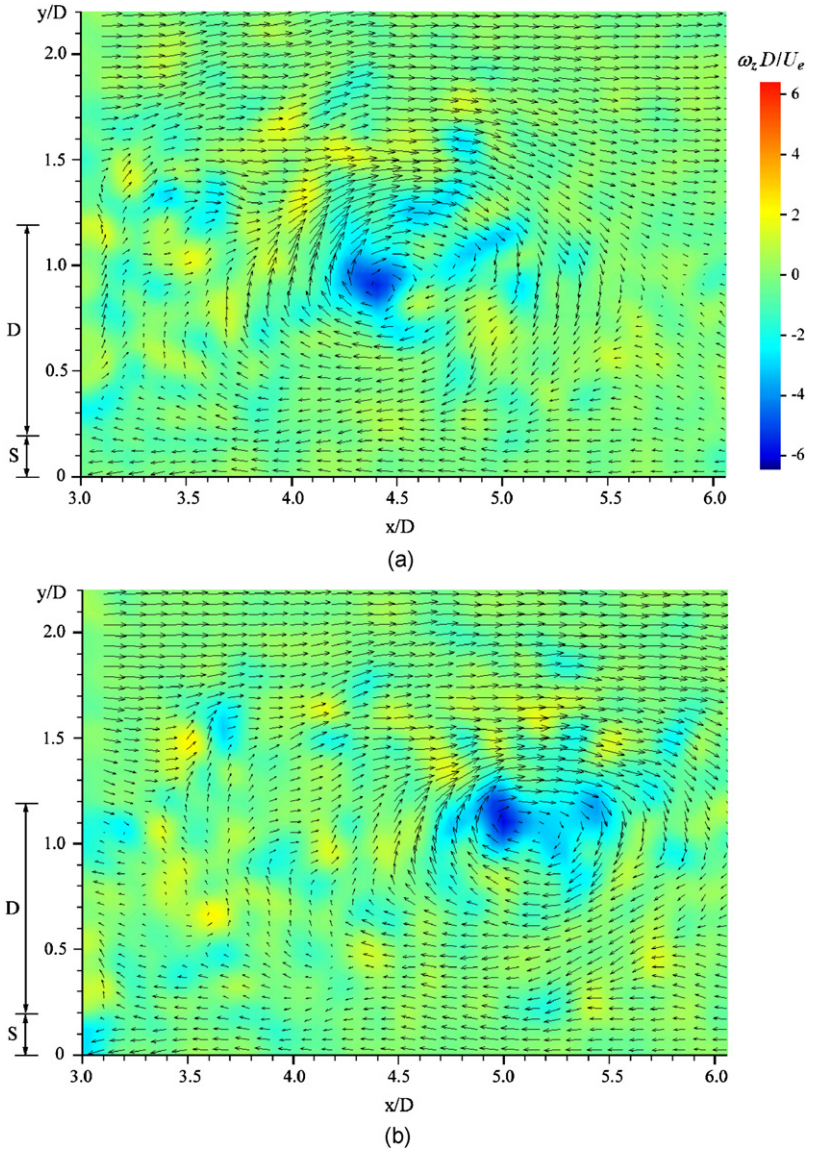

Fig. 16. Snapshots of the instantaneous field at the instant shown in Fig. 15: (a) ③ and (b) ④. Superimposed with contours of $\omega_z D/U_e$.

For $S/D = 0.3$ and 0.4, although positive vortices are shed periodically from the lower side of the cylinder, as shown in Fig. 12, they are relatively weak and have decayed significantly (or cannot be discriminated from the background noise), leaving the upper layer of negative vortices as the dominant features in region II, resembling to that of $S/D = 0.2$. The convection velocity of vortex is kept unchanged about $U_c = 0.5U_e$ in both cases.

The evolution of the vortical structures in region II for $S/D = 0.6$ is shown in Figs. 17 and 18. For this case, both layers of well-organized negative and positive vortices are evident, although the lower positive vortex is relatively smaller in size, as well as weaker in strength ($|\Gamma/(DU_e)| \approx 0.6$) as compared to the upper negative vortex ($|\Gamma/(DU_e)| \approx 1.1$, which is slightly higher than the corresponding value of 1.0 for $S/D = 0.2$). This scenario depicts a negative vortex moving from the left hand side to the right hand side of region II, during which a positive vortex is centred at $x/D \approx 5.2$ and 5.7, respectively, for the first two instants (① and ②); thereafter, a new positive vortex enters the viewing region from the fourth instant (④) onwards. Fig. 17(a) shows that the trajectories of the two layers of vortices keep nearly horizontal, with the same convection velocity of $0.5U_e$. Regarding their shape, the upper negative vortex becomes nearly circular for $S/D = 0.6$ (Fig. 18), as compared to that for $S/D = 0.2$ (Fig. 16) which is elliptic and

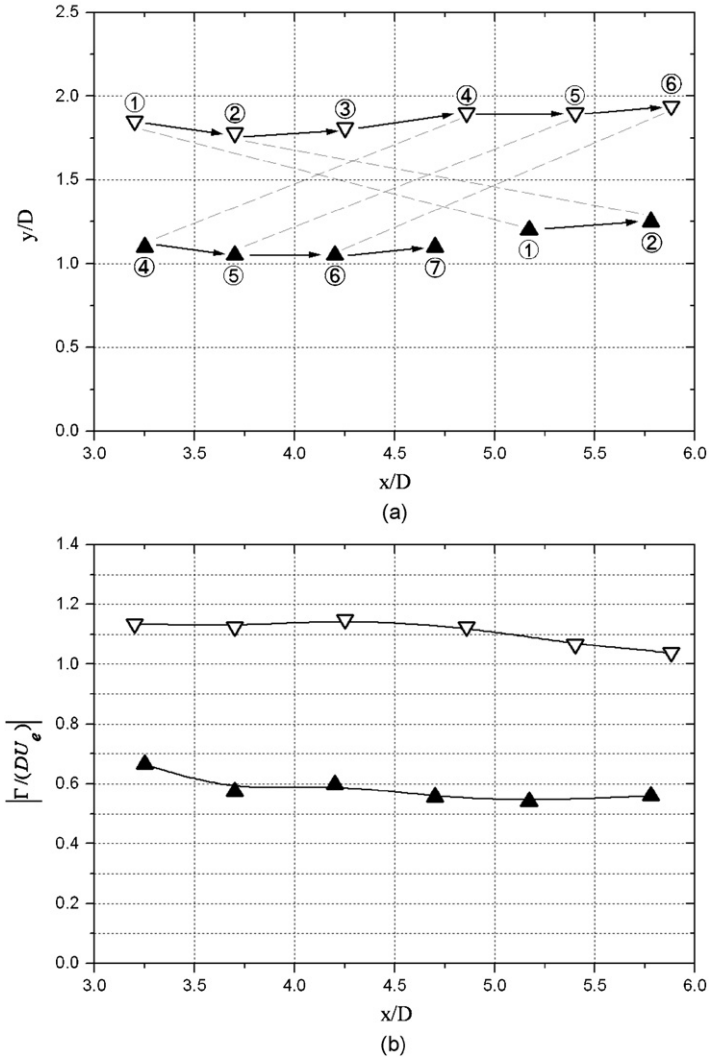

Fig. 17. Evolution of the shed discrete vortices for $S/D = 0.6$ in region II ($x/D = 3$–6): (a) trajectory and (b) circulation $|\Gamma/(DU_e)|$.

elongated in the streamwise direction; on the other hand, the lower positive vortex generally exhibits a vertically elongated elliptic shape, indicating the asymmetry of the flow. For even larger gap ratios ($S/D \geqslant 0.8$), the flow symmetry is roughly achieved, in that both layers of vortices are nearly circular in shape and the circulation of the positive vortex recovers to the same extent as that of the negative vortex.

The streamwise spacing (L_x) of successive vortices can be calculated using $L_x = U_c/f$, where f is the vortex shedding frequency. As shown above, both the convection velocity and the shedding frequency remain constant $U_c \approx 0.5U_e$ and $f \approx 3.1$ Hz for all the cases examined. Therefore, the value of L_x is also kept constant, which is about $2.7D$.

The above observations on region II illustrate that for small and intermediate gap ratios ($S/D \leqslant 0.6$), the shed discrete vortex is well-organized and regular with a constant convection velocity $U_c = 0.5U_e$ and a constant spacing $L_x = 2.7D$, which is virtually independent of S/D. In addition, although the vortex strength (in terms of vorticity and circulation levels) decays slightly with downstream distance over the range $3 < x/D < 6$, it keeps roughly constant in this range; this indicates that effects from other sources, on the vortex, may be negligible, including the wall/vortex interaction, the viscous effect, etc. However, the former (i.e. the wall/vortex interaction) should be evaluated, due to the presence of the wall in this flow configuration. Interactions between a discrete vortex and a flat wall have previously been established, see for example Doligalski et al. (1994). The characteristic parameter of the phenomenon is the

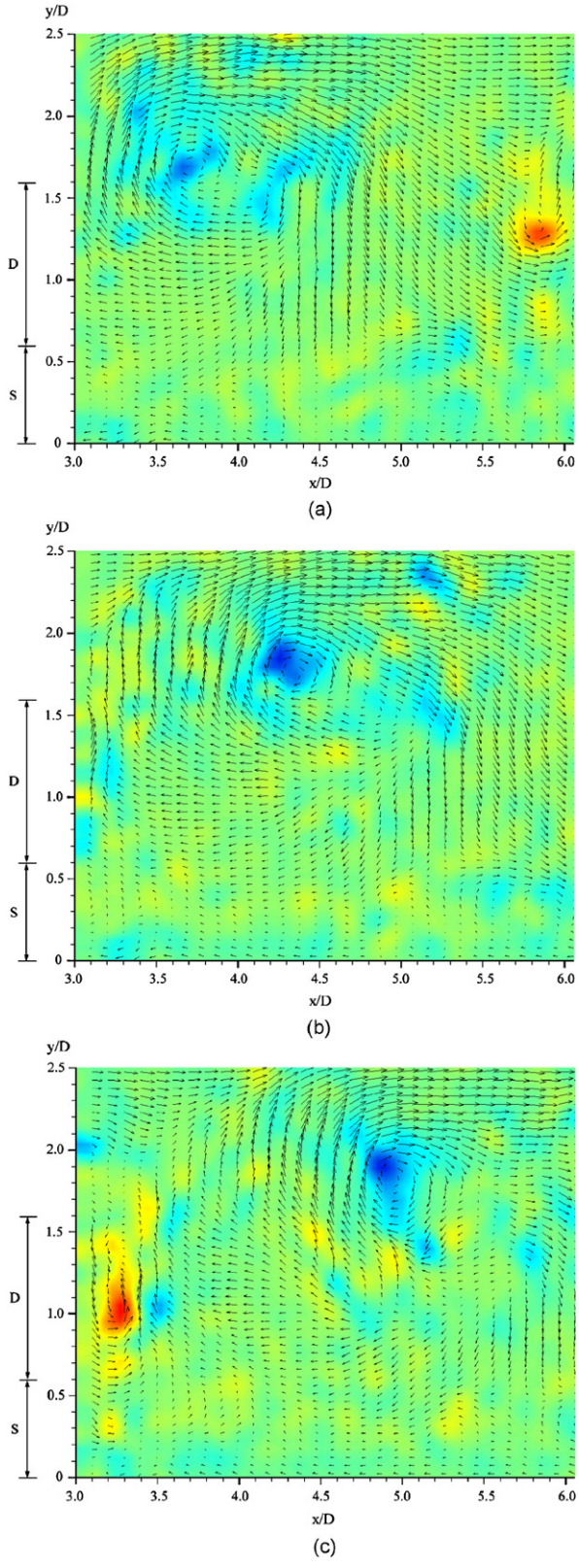

Fig. 18. Snapshots of the instantaneous field at the instant shown in Fig. 17: (a) ②, (b) ③, and (c) ④. Superimposed with contours of $\omega_z D/U_e$.

reduced circulation factor γ:

$$\gamma = \frac{\Gamma}{4\pi U_e h},$$

where h is the distance between the vortex centre and the wall. The interactions can be classified as a function of the value of γ: weak ($|\gamma| \leqslant 0.05$), moderate ($|\gamma| \leqslant 0.15$) and strong ($|\gamma| \leqslant 0.4$). In the present study, the $S/D = 0.2$ case is taken as an example, since in this case the distance h is the smallest (about $1D$) yet with very considerable strength ($\left|\Gamma/(DU_e)\right| \approx 1$). The calculated value of γ is -0.07 (the values of $|\gamma|$ for other gap ratios are about 0.04–0.07), falling in the weak-to-intermediate range, which indicates that the interactions between the vortex and the bottom wall are not significant.

4. Conclusions

PIV measurements have been conducted to investigate the flow structures in wake of a cylinder close to the water channel wall with varying gap ratios ($S/D = 0.1$–1.0), under a fixed Reynolds number of 1.2×10^4 and a fixed incident boundary layer thickness of $0.4D$. The data presented in this paper attempt to provide quantitative information on the statistical and dynamic features of this flow configuration. It is shown that flow structures are strongly dependent on the gap ratio. A general observation is that the principal features of the quantitative patterns move upstream with increasing value of S/D. As S/D increases from 0.1 to 0.4, the lengths of both the wake recirculation and the separating shear layer decrease substantially. Also, corresponding patterns of Reynolds stress contract towards the base of the cylinder, together with elevated values of Reynolds stress at upstream locations. These ensemble-averaged flow features are attributed to earlier onset of shear-layer transition in the instantaneous flow fields, from the steady K–H roll-ups for small values of S/D, to the periodic vortex shedding for large values of S/D. The critical gap ratio for vortex shedding $(S/D)_{\text{crit}}$ is 0.3.

While the wall effect on the flow gradually decreases and the vortex shedding becomes stronger with increasing S/D, the vortex shedding frequency remains constant at $\text{St} = 0.19$ for all the cases considered ($0.3 \leqslant S/D \leqslant 1.0$). When the gap ratio is large enough ($S/D \geqslant 0.8$), the wall effect can be neglected and the wake flow resembles: that of a stand-alone cylinder. For the intermediate gap ratios ($0.3 \leqslant S/D \leqslant 0.6$), the wall effect is significant, resulting in the flow asymmetry about the cylinder centreline. Within this gap ratio range, the wall boundary layer is also periodically destabilized by the shed vortices from the lower side of the cylinder. For small gap ratios ($S/D = 0.1$ and 0.2), on the other hand, the lower shear layer remains steady and does not curl up into a discrete vortex, and thus the periodic vortex shedding is suppressed. However, the flow patterns for $S/D = 0.1$ and 0.2 are different. For $S/D = 0.1$, no periodicity is found in neither shear layers. For $S/D = 0.2$, while the lower shear layer remains constant, there is periodicity in the upper shear layer with $\text{St} = 0.19$. Furthermore, the evolution of the shed vortex for two representative gap ratios ($S/D = 0.2$ and 0.6) is illustrated by a time series of the instantaneous flow field in region II ($3 < x/D < 6$). The shed vortex moves downstream basically parallel to the wall with a nearly constant convection velocity of $0.5U_e$ and streamwise spacing of $2.7D$. The strength of the shed vortex, in terms of vorticity and circulation levels, keeps nearly constant in this region, and the vortex/wall interactions are insignificant.

References

Adrian, R.J., 1991. Particle-imaging techniques for experimental fluid mechanics. Annual Review of Fluid Mechanics 23, 261–304.

Adrian, R.J., Meinhart, C.D., Tomkins, C.D., 2000. Vortex organization in the outer region of the turbulent boundary layer. Journal of Fluids Mechanics 422, 1–54.

Angrilli, F., Bergamaschi, S., Cossalter, V., 1982. Investigation of wall induced modifications to vortex shedding from a circular cylinder. ASME Journal of Fluids Engineering 104, 518–522.

Bearman, P.W., Zdravkovich, M.M., 1978. Flow around a circular cylinder near a plane boundary. Journal of Fluid Mechanics 89, 33–47.

Buresti, G., Lanciotti, A., 1992. Mean and fluctuating forces on a circular cylinder in cross-flow near a plane surface. Journal of Wind Engineering and Industrial Aerodynamics 41, 639–650.

Cantwell, B.J., Coles, D., 1983. An experimental study of entrainment and transport in the turbulent near wake of a circular cylinder. Journal of Fluid Mechanics 136, 321–374.

Choi, J.-H., Lee, S.-J., 2000. Ground effect of flow around an elliptic cylinder in a turbulent boundary layer. Journal of Fluids and Structures 14, 697–709.

Dipankar, A., Sengupta, T.K., 2005. Flow past a circular cylinder in the vicinity of a plane wall. Journal of Fluids and Structures 20, 403–423.

Doligalski, T.L., Smith, C.R., Walker, J.D.A., 1994. Vortex interactions with walls. Annual Review of Fluid Mechanics 26, 573–616.
Dong, S., Karniadakis, G.E., Ekmekci, A., Rockwell, D., 2006. A combined direct numerical simulation-particle image velocimetry study of the turbulent near wake. Journal of Fluid Mechanics 569, 185–207.
Forliti, D.J., Strykowski, P.J., Debatin, K., 2000. Bias and precision errors of digital particle image velocimetry. Experiments in Fluids 28, 436–447.
Grass, A.J., Raven, P.W.J., Stuart, R.J., Bray, J.A., 1984. The influence of boundary layer velocity gradients and bed proximity on vortex shedding from free spanning pipelines. ASME Journal of Energy Resources Technology 106, 70–78.
Hyun, B.S., Balachandar, R., Yu, K., Patel, V.C., 2003. Assessment of PIV to measure mean velocity and turbulence in open-channel flow. Experiments in Fluids 35, 262–267.
Jeong, J., Hussain, F., 1995. On the identification of a vortex. Journal of Fluid Mechanics 285, 69–94.
Lei, C., Cheng, L., Kavanagh, K., 1999. Re-examination of the effect of a plane boundary on force and vortex shedding of a circular cylinder. Journal of Wind Engineering and Industrial Aerodynamics 80, 263–286.
Price, S.J., Sumner, D., Smith, J.G., Leong, K., Païdoussis, M.P., 2002. Flow visualization around a circular cylinder near to a plane wall. Journal of Fluids and Structures 16, 175–191.
Raffel, M., Willert, C.E., Kompenhans, J., 1998. Particle Image Velocimetry: A Practical Guide. Springer, Berlin, Heidelberg, New York.
Robinson, S.K., 1991. Coherent motion in the turbulent boundary layer. Annual Review of Fluid Mechanics 23, 601–639.
Scarano, F., Riethmuller, M.L., 1999. Iterative multigrid approach in PIV image processing with discrete window offset. Experiments in Fluids 26, 513–523.
Taniguchi, S., Miyakoshi, K., 1990. Fluctuating fluid forces acting on a circular cylinder and interference with a plane wall. Experiments in Fluids 9, 197–204.
Vollmers, H., 2001. Detection of vortices and quantitative evaluation of their main parameters from experimental velocity data. Measurement Science and Technology 12, 1199–1207.
Wang, X.K., Tan, S.K., 2007. Experimental investigation of the interaction between a plane wall jet and a parallel offset jet. Experiments in Fluids 42, 551–562.